Scanned probe imaging of nanoscale magnetism at cryogenic temperatures with a single-spin quantum sensor

Matthew Pelliccione[1], Alec Jenkins[1], Preeti Ovartchaiyapong[1], Christopher Reetz[1], Eve Emmanouilidou[2], Ni Ni[2] and Ania C. Bleszynski Jayich[1]*

High-spatial-resolution magnetic imaging has driven important developments in fields ranging from materials science to biology. However, to uncover finer details approaching the nanoscale with greater sensitivity requires the development of a radically new sensor technology. The nitrogen–vacancy (NV) defect in diamond has emerged as a promising candidate for such a sensor on the basis of its atomic size and quantum-limited sensing capabilities. It has remained an outstanding challenge to implement the NV centre as a nanoscale scanning magnetic probe at cryogenic temperatures, however, where many solid-state systems exhibit non-trivial magnetic order. Here, we present NV magnetic imaging down to 6 K with $3\,\mu T\,Hz^{-1/2}$ field sensitivity, and use the technique to image vortices in the iron pnictide superconductor $BaFe_2(As_{0.7}P_{0.3})_2$ with critical temperature $T_c = 30$ K. The expansion of NV-based magnetic imaging to cryogenic temperatures will enable future studies of previously inaccessible nanoscale magnetism in condensed-matter systems.

Magnetism in condensed-matter systems often accompanies exotic electronic phases, and its presence is the basis for many advanced technologies. Examples include vortices in high-temperature superconductors[1], ferromagnetism at the interface between oxide band insulators[2] and skyrmion phases in helimagnets[3,4]. Many experimental tools, including real-space imaging techniques such as magnetic force microscopy (MFM)[5], scanning superconducting quantum interference devices (SQUIDs)[6] and Lorentz transmission electron microscopy (TEM)[7] as well as reciprocal space techniques including neutron scattering[8] have been successfully used to study magnetism in these systems. However, each of these techniques has limitations that must be considered. In MFM, a ferromagnetic tip must be placed in close proximity to a sample, which can perturb the magnetic order that is being probed. Scanning SQUIDs typically require a probe temperature of 10 K or lower and generally offer micrometre-size spatial resolution, although recent studies have enhanced the resolution to submicrometre scales[9]. Lorentz TEM can provide images with high spatial resolution and magnetic contrast, but requires very thin samples—typically less than 100 nm thick. Neutron scattering requires the growth of large, high-purity single-crystal samples, and is an ensemble-averaged measurement. There is therefore a significant need to develop a real-space, non-invasive magnetic sensor that is capable of studying magnetic order at sub-10 nm spatial resolution and sub-$\mu T\,Hz^{-1/2}$ d.c. field sensitivities.

The NV defect centre in diamond is an exceptionally versatile single-spin system with unique quantum properties that have driven its application in diverse areas ranging from quantum information and photonics to quantum metrology[10–19]. Cryogenic scanning magnetometry stands out as potentially the most impactful application of NV centres, taking advantage of the exquisite magnetic field sensitivity and intrinsic atomic scale of the NV centre for high-resolution imaging[20]. The operation of an NV-based magnetic probe is dependent on a fundamentally different sensing principle than other imaging methods, namely the spin-dependent photoluminescence of a solid-state defect. The NV centre has recently been proposed[21–23] and demonstrated[24–29] as a scanning magnetometer in a number of different contexts, but has been restricted to room-temperature operation. However, NV centres maintain their high field sensitivity over a large temperature range—from cryogenic to ambient and above[15,30]—and hence are ideal for imaging nanoscale magnetism through orders of magnitude in temperature. A cryogenic NV scanning magnetometer enables the study of a host of new systems that could benefit from a highly sensitive nanoscale probe, particularly solid-state systems with non-trivial magnetic order or magnetic phase transitions at low temperature.

In this work, we demonstrate the operation of an NV scanning magnetometer down to 6 K with sub-100 nm spatial resolution and $3\,\mu T\,Hz^{-1/2}$ d.c. field sensitivity. We use the scanning NV probe to image vortices in an iron pnictide superconductor and magnetic domains in a hard disk, highlighting the compatibility of the technique with cryogenic condensed-matter phenomena. We also discuss the prospects for improving the spatial resolution and field sensitivity of the probe, which are limited by the separation of the NV centre from the sample and the coherence time of the NV centre, respectively. With the coherence properties that have been demonstrated for shallow NV centres in bulk diamond[31,32], it is reasonable to expect that with modest improvements to the scanning probes presented here, the technique could reach $40\,nT\,Hz^{-1/2}$ d.c. and $10\,nT\,Hz^{-1/2}$ a.c. field sensitivities.

Single-spin microscope

A schematic representation of the system is shown in Fig. 1a. A nanofabricated single-crystal diamond cantilever with an NV centre near the apex of the tip is used as the probe in a custom-built, low-temperature atomic force microscope (AFM). The cantilever consists of an array of tips containing NV centres, where a

[1]Department of Physics, University of California Santa Barbara, Santa Barbara, California 93106, USA. [2]Department of Physics & Astronomy, University of California Los Angeles, Los Angeles, California 90095, USA. *e-mail: ania@physics.ucsb.edu

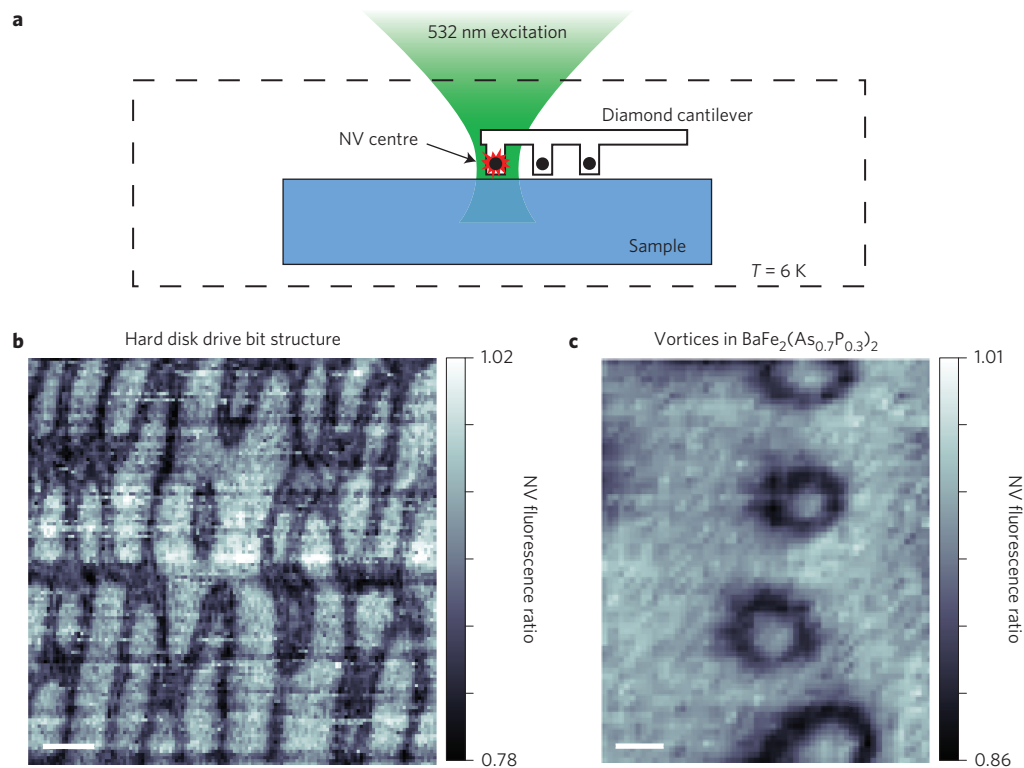**Figure 1 | Cryogenic NV scanning probe magnetometry. a**, The scanning probe is an NV centre at the apex of a tip on a diamond cantilever. The cantilever contains an array of tips where only one is selected for imaging. Both the NV centre and sample are housed in a closed-cycle cryostat with a base temperature of 6 K. A 532 nm laser is focused on the NV centre and the resulting fluorescence contains information about the stray magnetic field of the sample as it is scanned below the tip. Microwave excitation is applied via a gold wirebond located within 50 μm of the NV centre. **b**, NV magnetometry image of the bits of a hard disk at $T = 6$ K. The dark contours in the image correspond to locations where the stray field from the hard disk has a magnitude of 5.3 G (resonant with a 2892.7 MHz RF field) along the axis of the NV centre. Scale bar, 100 nm. **c**, NV magnetometry image of vortices in the superconductor $BaFe_2(As_{0.7}P_{0.3})_2$ at $T = 6$ K. Analogous to **b**, dark features correspond to the 5.9 G magnetic field contours (2,862 MHz RF field). Vortices were formed by cooling the sample through its superconducting transition ($T_c = 30$ K) in a 10 G external field. Scale bar, 400 nm.

single tip is selected for imaging during a given measurement. The closed-cycle cryostat (Montana Instruments) reaches a base temperature of 4.3 K. However, in our experiment, the sample temperature is typically 6 K due to a combination of heating from the microwave excitation needed for spin manipulation and an intentionally reduced cooling power to minimize tip–sample vibrations. The AFM is comprised of a coarse positioning stage with six degrees of freedom (Janssen Precision Engineering) that allows for independent alignment of the tip with the sample and of the confocal microscope optics with the NV centre on the tip. A piezo scanner (Attocube ANSxyz100hs) mounted on the coarse positioning stage allows for a 9 μm sample scan range at base temperature. The root mean square (RMS) AFM vibration between the tip and the sample in the vertical direction with the fridge running is 0.72 nm in a 1 kHz bandwidth, measured with a tapping mode technique[33]. Long-term tip–sample drift is less than 10 nm over a period of several days, a consequence of the cryogenic environment and the temperature stability of the system. The closed-cycle nature of the cryostat also has an important advantage over liquid cryogen-based designs as it eliminates liquid cryogen handling, which can severely interrupt scanning probe measurements. A window-corrected objective (Olympus LCPLFN50xLCD, 0.7 NA, 3 mm working distance) that resides outside the cryostat is used for NV optical excitation and fluorescence collection, and is separated from the AFM by a pair of 200 μm thick BK7 windows, one at 300 K and the other at 40 K, to act as radiation shields. Two representative low-temperature magnetic images acquired with the NV scanning probe at $T = 6$ K are shown in Fig. 1b,c. Individual bits on a magnetic hard drive are shown in Fig. 1b,

with a bit size consistent with MFM scans taken at room temperature (Supplementary Information). Vortices in the superconductor $BaFe_2(As_{0.7}P_{0.3})_2$ ($T_c = 30$ K) are shown in Fig. 1c. In both images, dark features trace the contours of constant magnetic field.

Probe design and fabrication

Figure 2a shows a scanning electron microscope (SEM) image of a typical single-crystal diamond cantilever used in this work. Monolithic diamond probes were chosen over diamond nanocrystals attached to silicon AFM tips because of the superior coherence properties afforded by the bulk diamond substrate. Approximately 100 of these cantilevers were fabricated on a (100)-oriented 2×2 mm diamond substrate bonded to an oxidized silicon wafer using a diamond-on-insulator approach[34]. The pillars were formed with nanoimprint lithography using a Ti hard mask and O_2 etching, and are approximately 200 nm in diameter, 1 μm tall and have a 1 μm pitch. The free-standing probes were then released with a deep reactive-ion etch through the silicon substrate. The density of the NV centres was chosen to yield on average one NV centre per pillar at a depth of 15–20 nm, with ^{14}N implantation performed at a dose of 5×10^{11} per cm^2 at an energy of 15 keV. This was followed by annealing at 850 °C in vacuum and cleaning in a boiling sulfuric acid/nitric acid mixture. The rather unconventional AFM probe design (with an array of tips) was chosen to increase the probability of finding a shallow NV centre with favourable coherence properties. The trade-off in this design is that any given pillar may not be in direct contact with the sample surface due to geometric constraints, for example if another pillar touches the surface first. However, the array of pillars could potentially
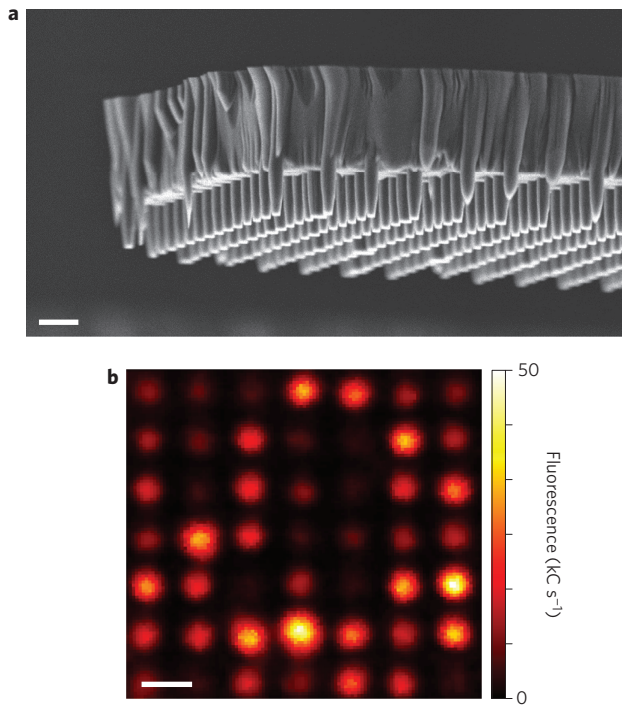
Figure 2 | Single-crystal diamond AFM probes. a, SEM image of a typical diamond cantilever fabricated for magnetometry. Each full cantilever measures $150 \times 20 \times 3$ μm. On average, there is approximately one NV centre per pillar. Scale bar, 1 μm. **b**, Confocal microscopy image of an array of pillars on a cantilever showing NV fluorescence from a majority of pillars. A green excitation power of 30 μW was used. Scale bar, 1 μm.

provide significant imaging enhancements in a wide-field imaging scheme where several pillars are measured simultaneously to image large areas quickly, and provide vector-field magnetometry if NV centres of different crystallographic orientations are used.

A confocal fluorescence image of a typical diamond cantilever is shown in Fig. 2b, with 30 μW green excitation power incident on the back aperture of the objective. The relatively high fluorescence rates are a consequence of optical waveguiding by the diamond pillar structure[35], where fluorescence saturation is typically around 500 kC s^{-1} at incident green powers of about 1 mW. We choose to carry out measurements at lower incident green powers to ensure that laser heating is insignificant, although this may not be necessary depending on the properties of the sample being measured. Two-photon autocorrelation measurements verified which pillars host single NV centres[36]. Using a micromanipulator the diamond cantilevers are glued to a pulled glass fiber, which is then attached to a quartz tuning fork for force sensing. The tuning fork is anchored in the shear mode to reduce the overall height of the tip assembly to less than 600 μm, which allows room for the cryostat window and radiation shield to fit within the working distance of the microscope objective.

Cryogenic magnetic imaging

We demonstrate two complementary imaging modes for the NV magnetometer in Fig. 3. All of the data presented in the figure were taken at 6 K on a hard disk sample. A quantitative image of the magnetic field strength at every point in the scan (a 'full-field' image) can be obtained by taking the full electron spin resonance (ESR) response of the NV centre at each position in the scan. The result of such a measurement is shown in Fig. 3a, where B_{NV}, the magnetic field along the NV axis, is plotted and obtained by measuring the frequency splitting between the two ESR peaks, $\Delta f = 2\gamma |B_{NV}|$, where $\gamma = 2.8$ MHz G^{-1} is the gyromagnetic ratio of

the NV electronic spin. This splitting only sets the magnitude of the field $|B_{NV}|$; the sign of the field can be determined by applying a small external field perpendicular to the sample (± 5 G) and monitoring how the ESR splitting changes in different regions of the scan. This method has a large dynamic field range (set by the bandwidth of the ESR spectrum) but is relatively slow. In Fig. 3a, the dynamic field range during the measurement is ± 54 G, each point represents 7.5 s of averaging and the field sensitivity is 30 μT Hz$^{-1/2}$, which is calculated using the error in the fit of the peak positions in the ESR spectrum, along with the acquisition time per point. We note that by fitting the full ESR response it is possible to extract more information than just $|B_{NV}|$. These parameters include the linewidth of the peaks, limited by the free induction decay time T_2^* in the low radio frequency (RF) power limit, and the field magnitude perpendicular to the NV axis $|B_\perp|$, although this method is only sensitive to $|B_\perp|$ to second order. Measurements of T_2^* are useful in decoherence imaging[37,38] where T_2^* may be reduced by magnetic noise on the surface of the sample.

The second magnetic imaging method is outlined in Fig. 3b. This method is sensitive to a particular magnetic field contour B_c, which is chosen by the frequency of the RF excitation f_{RF} applied during the measurement, and $B_c = \gamma(f_{RF} - f_{ZFS})$, where $f_{ZFS} = 2.878$ GHz is the NV zero field splitting at 6 K. The contour imaging method is faster than full-field imaging and therefore has a better field sensitivity at the expense of a reduced dynamic range, which is set by the width of the ESR transition and ultimately T_2^*. In Fig. 3b, the experimentally determined field sensitivity is 3 μT Hz$^{-1/2}$, with 0.6 s of averaging per point. To mitigate slow fluctuations in the fluorescence that are unrelated to the magnetic signal, the microwave excitation is cycled repeatedly on for 10 μs and then off for 10 μs at each point in the scan, and the ratio is plotted. The preservation of the magnetic structure and its equivalent position in the scans shown in Fig. 3a,b, which were acquired several days apart, highlights the long-term stability and non-invasiveness of the imaging system. The contour imaging method was also used to obtain the data in Fig. 1b,c.

Figure 4 demonstrates the nanoscale spatial resolution we have achieved with our NV scanning probe. Figure 4a is a magnetic contour image ($B_c = 7.9$ G) of a hard disk at $T = 6$ K, with a corresponding linecut shown in Fig. 4b (point spacing of 6 nm). From the linecut, the magnetic field at two points separated by 6 nm is well resolved within the error of the measurement. However, this does not necessarily correspond to the smallest magnetic domain resolvable in the scan, only the resolvable field gradient in the plane of the NV sensor. The ultimate resolution of the image in Fig. 4a, which clearly shows domains under 100 nm in size, will depend also on the separation of the NV centre from the surface during the scan. When compared with the contour image in Fig. 3b, the contours in Fig. 4a are sharper due to a reduced NV–sample separation, which results in larger magnetic field gradients in the imaging plane. The spatial resolution of the imaging method, δx, is ultimately determined by the magnetic field gradient $\nabla_x B_{NV}$ and the linewidth of the NV ESR transition $\delta f = 1/T_2^*$, $\delta x = (T_2^* \cdot \gamma \nabla_x B_{NV})^{-1}$. In these measurements, $T_2^* = 250$ ns and $\nabla_x B_{NV} \approx 0.25$ G nm^{-1} at the location of the contours. Importantly, Fig. 4 shows that mechanical vibrations and drift during the measurement are well below 6 nm.

Magnetometry images of vortices in the iron pnictide superconductor BaFe$_2$(As$_{0.7}$P$_{0.3}$)$_2$ at 6 K are shown in Fig. 5a,b. The images were taken with the contour imaging method. The sample was cooled through its superconducting transition ($T_c = 30$ K) in a 10 G magnetic field applied perpendicular to the ab plane of the sample. The dark circular features, which correspond to field contours of 5.9 G (Fig. 5a) and 8.8 G (Fig. 5b), are due to the stray field from the two vortices in each figure. The contours shrink in size when comparing Fig. 5a,b, as the NV must be brought closer to the centre of the vortex to match the higher magnetic field ESR
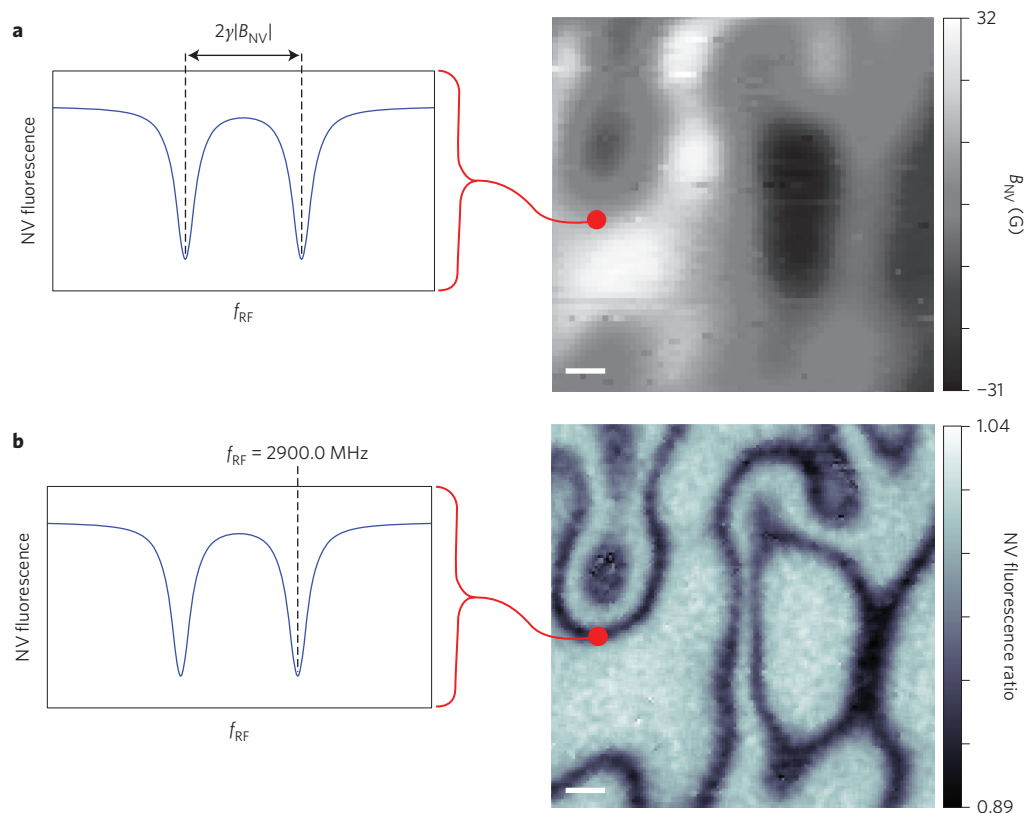
Figure 3 | Comparison of magnetic imaging protocols. Images are taken of a magnetic hard drive at $T = 6$ K. **a**, A full ESR curve is acquired at each position in the scan by measuring the NV fluorescence as a function of RF excitation frequency. The image on the right shows B_{NV}, the magnetic field along the NV axis, where $|B_{NV}|$ is proportional to the ESR peak splitting and the sign of the field is extracted as described in the text. Scale bar, 100 nm. The ESR spectrum at the position of the red dot is shown on the left. **b**, Dark features correspond to contours of constant $|B_{NV}| = 7.9$ G, obtained when the field is on resonance with a fixed RF excitation frequency ($f_{RF} = 2,900.0$ MHz). The relative change in NV fluorescence as a result of the RF drive is plotted. Scale bar, 100 nm. The images in **a**,**b** are taken over the same area of the hard disk sample.

resonance condition. The measured vortex density, estimated using the larger scan area in Fig. 1c, is approximately $0.45 \pm 0.1\ \mu m^{-2}$. This value is consistent with the calculated vortex density of $(10\ G)/\Phi \approx 0.5\ \mu m^{-2}$ assuming each vortex is associated with one magnetic flux quantum $\Phi = h/(2e)$. As another confirmation of the superconducting nature of the signal, the measured magnetic response disappears when the sample is heated above $T_c = 30$ K. We note that NV centres in bulk diamond have been used to study the presence of the superconducting state via Meissner screening[39,40], although not in the context of vortex imaging.

Figure 5c,d shows simulations of the images in Fig. 5a,b using the computed field profile from a superconducting vortex[41] and the properties of the NV centre used in the measurement. The slight asymmetry of the features, most noticeable in Fig. 5a, is well captured by the simulations and is a result of the fact that the axis of the NV centre is tilted 35.3° from the plane of the sample. Two important input parameters for the simulation are the London penetration depth λ of the superconductor, and the NV–sample separation h_{NV}. If h_{NV} can be determined independently, for example by imaging a magnetic reference sample[28], the NV imaging

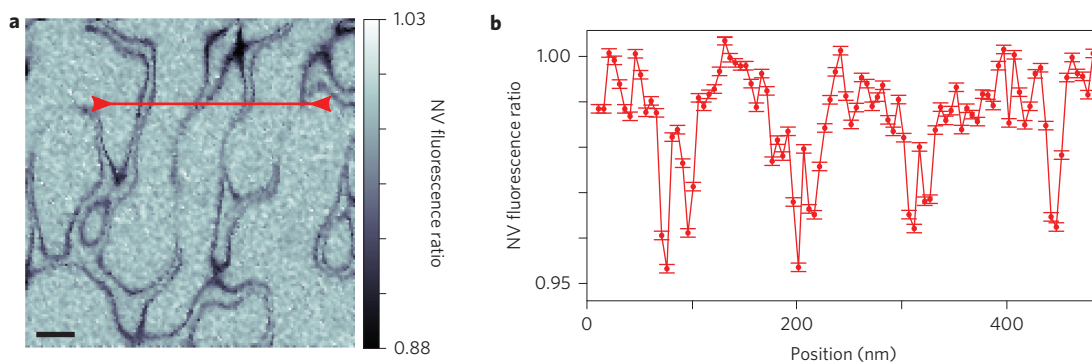**Figure 4 | High-spatial-resolution magnetic imaging at $T = 6$ K. a**, Magnetic field contour image of a hard disk (7.9 G, 2,900.0 MHz RF excitation). Scale bar, 100 nm. **b**, One-dimensional line-cut along the red line in **a**. Features in the imaging plane are clearly resolved down to a spatial resolution of 6 nm, which is set by the point spacing in the scan. This data highlights the nanoscale spatial resolution of the NV sensor and the vibrational stability of the cryogenic imaging system. The error bars reflect one standard deviation confidence intervals due to photon counting statistics.
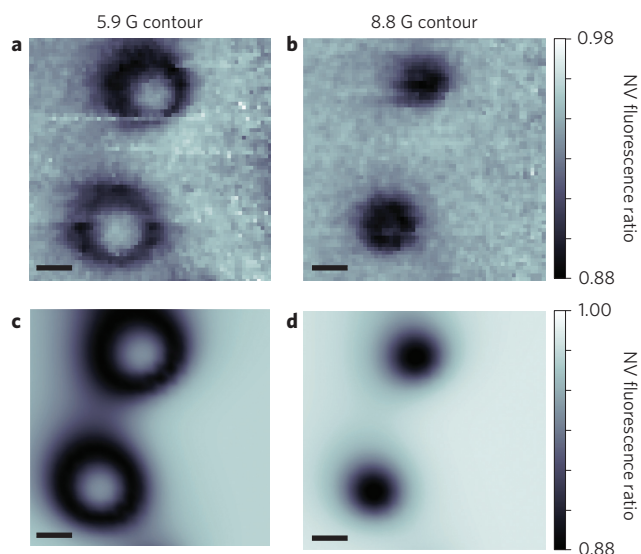
Figure 5 | NV magnetometry of vortices in the iron pnictide superconductor BaFe$_2$(As$_{0.7}$P$_{0.3}$)$_2$ at T = 6 K. a,b, Magnetic images corresponding to the 5.9 G (**a**) and 8.8 G (**b**) contours of constant magnetic field. Scale bars, 200 nm. The sample was cooled in a 10 G field applied perpendicular to the sample through the superconducting transition at T_c = 30 K to form vortices. The dark circular features indicate the location of the vortices. **c,d**, Simulated field contours at 5.9 G (**c**) and 8.8 G (**d**) from a vortex pair as measured by an NV centre located 330 nm above the surface. Scale bars, 200 nm. λ is assumed to be 200 nm in the simulation, with the NV centre oriented along the [111] axis of the [100]-cut diamond tip. The elongation of the vortex contours in **a** and **c** is a consequence of the stray field from adjacent vortices and the non-orthogonal orientation of the NV with respect to the sample plane.

method provides a direct way of measuring λ by fitting the results of the simulation to the contour images. Conversely, if λ is known, h_{NV} can be extracted. In our analysis, we set λ = 200 nm based on previous measurements[42,43], which yields h_{NV} = 330 nm to most closely fit the data in Fig. 5a,b.

Conclusion

We have presented the first cryogenic NV scanning magnetometry images and demonstrated sub-100 nm spatial resolution and 3 µT Hz$^{-1/2}$ field sensitivity down to 6 K. Combining the excellent spatial resolution and sensitivity of the NV with cryogenic operation opens the door to the study of a variety of low-temperature condensed-matter phenomena. Although vortex structures have been probed with other magnetic imaging techniques[44,45], our demonstration is important because it highlights both the high spatial resolution of NV imaging at low temperature and the compatibility of the NV measurement protocol with the delicate nature of the superconducting state. As a result, studies that could benefit from this technique include probing the existence of time-reversal symmetry-broken states in high-T_c superconductors[46], determining the nanoscale structure of half-skyrmions in Cu$_2$OSeO$_3$[47] and understanding the origin of magnetism at the interface of rare-earth titanates and aluminates with SrTiO$_3$[48]. Future improvements will focus on extending the NV spin coherence times, along with engineering shallower NV centres to improve spatial imaging resolution. Using the full array of diamond pillars on the tip for wide-field imaging will require in situ control of the cantilever tilt relative to the sample, ensuring that all pillars are close enough to the surface to yield useful imaging data. In addition, an optimized design of the diamond pillars will increase photon counts via more efficient waveguiding of the NV fluorescence[49], leading to

faster acquisition times and an improved sensitivity. For example, a 10-nm deep NV centre with $T_2^\star$ = 25 µs and a photon collection rate of 500 kC s^{-1} will yield a d.c. field sensitivity of 40 nT Hz$^{-1/2}$. In pushing towards higher spatial resolutions with shallower NV centres, surface decoherence mechanisms—which reduce $T_2^\star$ and hence sensitivity[50]—must be considered. With a.c. sensing protocols that employ dynamical decoupling sequences to extend coherence times, a 2-nm deep NV[31] with T_2 = 5 µs will allow for sub-nanometre-scale imaging and an a.c. sensitivity of 100 nT Hz$^{-1/2}$. The a.c. protocols can also take advantage of the fast response time of the NV centre to image microwave magnetic fields[18]. As a result, the NV scanning magnetometer is an ideal probe for a wide range of high-resolution magnetic imaging studies of solid-state systems that are not possible with the established magnetic imaging toolset.

References

1. Lake, B. *et al.* Spins in the vortices of a high-temperature superconductor. *Science* **291,** 1759–1762 (2001).
2. Brinkman, A. *et al.* Magnetic effects at the interface between non-magnetic oxides. *Nature Mater.* **6,** 493–496 (2007).
3. Nagaosa, N. & Tokura, Y. Topological properties and dynamics of magnetic skyrmions. *Nature Nanotech.* **8,** 899–911 (2013).
4. Muhlbauer, S. *et al.* Skyrmion lattice in a chiral magnet. *Science* **323,** 915–919 (2009).
5. Milde, P. *et al.* Unwinding of a skyrmion lattice by magnetic monopoles. *Science* **340,** 1076–1080 (2013).
6. Kalisky, B. *et al.* Critical thickness for ferromagnetism in LaAlO$_3$/SrTiO$_3$ heterostructures. *Nature Commun.* **3,** 922 (2012).
7. Yu, X. Z. *et al.* Real-space observation of a two-dimensional skyrmion crystal. *Nature* **465,** 901–904 (2010).
8. Christianson, A. D. *et al.* Unconventional superconductivity in Ba$_{0.6}$K$_{0.4}$Fe$_2$As$_2$ from inelastic neutron scattering. *Nature* **456,** 930–932 (2008).
9. Vasyukov, D. *et al.* A scanning superconducting quantum interference device with single electron spin sensitivity. *Nature Nanotech.* **8,** 639–644 (2013).
10. Van der Sar, T. *et al.* Decoherence-protected quantum gates for a hybrid solid-state spin register. *Nature* **484,** 82–86 (2012).
11. Buckley, B. B. *et al.* Spin-light coherence for single-spin measurement and control in diamond. *Science* **330,** 1212–1215 (2010).
12. Maurer, P. C. *et al.* Room-temperature quantum bit memory exceeding one second. *Science* **336,** 1283–1286 (2012).
13. Neumann, P. *et al.* Single-shot readout of a single nuclear spin. *Science* **329,** 542–544 (2010).
14. Faraon, A. *et al.* Resonant enhancement of the zero-phonon emission from a colour centre in a diamond cavity. *Nature Photon.* **5,** 301–305 (2011).
15. Toyli, D. M., de las Casas, C. F., Christle, D. J., Dobrovitski, V. V. & Awschalom, D. D. Fluorescence thermometry enhanced by the quantum coherence of single spins in diamond. *Proc. Natl Acad. Sci. USA* **110,** 8417–8421 (2013).
16. Dolde, F. *et al.* Electric-field sensing using single diamond spins. *Nature Phys.* **7,** 459–463 (2011).
17. Staudacher, T. *et al.* Nuclear magnetic resonance spectroscopy on a (5-nanometer)^3 sample volume. *Science* **339,** 561–563 (2013).
18. Mamin, H. J. *et al.* Nanoscale nuclear magnetic resonance with a nitrogen vacancy spin sensor. *Science* **339,** 557–560 (2013).
19. Ovartchaiyapong, P., Lee, K. W., Myers, B. A. & Jayich, A. C. B. Dynamic strain-mediated coupling of a single diamond spin to a mechanical resonator. *Nature Commun.* **5,** 4429 (2014).
20. Rondin, L. *et al.* Magnetometry with nitrogen–vacancy defects in diamond. *Rep. Prog. Phys.* **77,** 056503 (2014).
21. Chernobrod, B. M. & Berman, G. P. Spin microscope based on optically detected magnetic resonance. *J. Appl. Phys.* **97,** 014903 (2005).
22. Degen, C. L. Scanning magnetic field microscope with a diamond single spin sensor. *Appl. Phys. Lett.* **92,** 243111 (2008).
23. Taylor, J. M. *et al.* High-sensitivity diamond magnetometer with nanoscale resolution. *Nature Phys.* **4,** 810–816 (2008).
24. Pelliccione, M., Myers, B. A., Pascal, L. M. A., Das, A. & Bleszynski Jayich, A. C. Two-dimensional nanoscale imaging of gadolinium spins via scanning probe relaxometry with a single spin in diamond. *Phys. Rev. Appl.* **2,** 054014 (2014).
25. Balasubramanian, G. *et al.* Nanoscale imaging magnetometry with diamond spins under ambient conditions. *Nature* **455,** 648–651 (2008).
26. Maletinsky, P. *et al.* A robust scanning diamond sensor for nanoscale imaging with single nitrogen-vacancy centres. *Nature Nanotech.* **7,** 320–324 (2012).

27. Grinolds, M. S. *et al.* Nanoscale magnetic imaging of a single electron spin under ambient conditions. *Nature Phys.* **9**, 215–219 (2013).
28. Rondin, L. *et al.* Stray-field imaging of magnetic vortices with a single diamond spin. *Nature Commun.* **4**, 2279 (2013).
29. Tetienne, J.-P. *et al.* Nanoscale imaging and control of domain-wall hopping with a nitrogen-vacancy center microscope. *Science* **344**, 1366–1369 (2014).
30. Toyli, D. M. *et al.* Measurement and control of single nitrogen-vacancy center spins above 600 K. *Phys. Rev. X* **2**, 031001 (2012).
31. Loretz, M., Pezzagna, S., Meijer, J. & Degen, C. L. Nanoscale nuclear magnetic resonance with a 1.9-nm-deep nitrogen-vacancy sensor. *Appl. Phys. Lett.* **104**, 033102 (2014). .
32. Favaro de Oliveira, F. *et al.* Effect of low-damage inductively coupled plasma on shallow nitrogen-vacancy centers in diamond. *Appl. Phys. Lett.* **107**, 073107 (2015).
33. Pelliccione, M., Sciambi, A., Bartel, J., Keller, A. J. & Goldhaber-Gordon, D. Design of a scanning gate microscope for mesoscopic electron systems in a cryogen-free dilution refrigerator. *Rev. Sci. Instrum.* **84**, 033703 (2013).
34. Ovartchaiyapong, P., Pascal, L. M. A., Myers, B. A., Lauria, P. & Bleszynski Jayich, A. C. High quality factor single-crystal diamond mechanical resonators. *Appl. Phys. Lett.* **101**, 163505 (2012).
35. Hausmann, B. J. M. *et al.* Single-color centers implanted in diamond nanostructures. *New J. Phys.* **13**, 045004 (2011).
36. Meijer, J. *et al.* Generation of single color centers by focused nitrogen implantation. *Appl. Phys. Lett.* **87**, 261909 (2005).
37. Luan, L. *et al.* Decoherence imaging of spin ensembles using a scanning single-electron spin in diamond. *Sci. Rep.* **5** (2015).
38. Cole, J. H. & Hollenberg, L. C. L. Scanning quantum decoherence microscopy. *Nanotechnology* **20**, 495401 (2009).
39. Bouchard, L. S., Acosta, V. M., Bauch, E. & Budker, D. Detection of the Meissner effect with a diamond magnetometer. *New J. Phys.* **13**, 025017 (2011).
40. Waxman, A. *et al.* Diamond magnetometry of superconducting thin films. *Phys. Rev. B* **89**, 054509 (2014).
41. Pearl, J. Structure of superconductive vortices near a metal-air interface. *J. Appl. Phys.* **37**, 4139–4141 (1966).
42. Hashimoto, K. *et al.* A sharp peak of the zero-temperature penetration depth at optimal composition in BaFe$_2$(As$_{1-x}$P$_x$)$_2$. *Science* **336**, 1554–1557 (2012).
43. Demirdis, S. *et al.* Disorder, critical currents, and vortex pinning energies in isovalently substituted BaFe$_2$(As$_{1-x}$P$_x$)$_2$. *Phys. Rev. B* **87**, 094506 (2013).
44. Yin, Y. *et al.* Scanning tunneling spectroscopy and vortex imaging in the iron pnictide superconductor BaFe$_{1.8}$Co$_{0.2}$As$_2$. *Phys. Rev. Lett.* **102**, 097002 (2009).
45. Gutierrez, J. *et al.* Scanning Hall probe microscopy of unconventional vortex patterns in the two-gap MgB$_2$ superconductor. *Phys. Rev. B* **85**, 094511 (2012).
46. Håkansson, M., Löfwander, T. & Fogelström, M. Spontaneously broken time-reversal symmetry in high-temperature superconductors. *Nature Phys.* **11**, 755–760 (2015).
47. Janson, O. *et al.* The quantum nature of skyrmions and half-skyrmions in Cu$_2$OSeO$_3$. *Nature Commun.* **5**, 5376 (2014).
48. Jackson, C. A., Zhang, J. Y., Freeze, C. R. & Stemmer, S. Quantum critical behaviour in confined SrTiO$_3$ quantum wells embedded in antiferromagnetic SmTiO$_3$. *Nature Commun.* **5**, 4258 (2014).
49. Momenzadeh, S. A. *et al.* Nanoengineered diamond waveguide as a robust bright platform for nanomagnetometry using shallow nitrogen vacancy centers. *Nano Lett.* **15**, 165–169 (2015).
50. Myers, B. A. *et al.* Probing surface noise with depth-calibrated spins in diamond. *Phys. Rev. Lett.* **113**, 027602 (2014).

Acknowledgements

Author contributions

M.P. and A.J. designed the experimental apparatus, carried out the experiments and analysed the data. A.J. and C.R. performed the simulations. P.O. fabricated the diamond probes. E.E. and N.N. provided the iron pnictide sample. M.P. and A.C.B.J. wrote the paper with feedback from all authors. A.C.B.J. supervised the project.

Additional information

Supplementary information is available in the online version of the paper. Reprints and permissions information is available online at www.nature.com/reprints. Correspondence and requests for materials should be addressed to A.C.B.J.

Competing financial interests

The authors declare no competing financial interests.